

PAPER • **OPEN ACCESS**

Simulation of runaway electron production with CQL3D coupled to NIMROD

To cite this article: Yu.V. Petrov *et al* 2022 *Nucl. Fusion* **62** 096009

View the [article online](#) for updates and enhancements.

You may also like

- [Numerical simulation of the hot-tail runaway electron production mechanism using CQL3D and comparison with Smith–Verwichte analytical model](#)
Yu V Petrov, P B Parks and R W Harvey
- [Simulation of the Ohkawa-mechanism-dominated current drive of electron cyclotron waves using linear and quasi-linear models](#)
P W Zheng, L H He, L Yin et al.
- [The effects of the scattering by edge plasma density fluctuations on lower hybrid wave propagation](#)
N Bertelli, G Wallace, P T Bonoli et al.

Simulation of runaway electron production with CQL3D coupled to NIMROD

Yu.V. Petrov^{1,*} , C.C. Kim², L.L. Lao³  and R.W. Harvey¹

¹ CompX, PO Box 2672, Del Mar, CA 92014-5672, United States of America

² SLS2 Consulting, San Diego, CA 92107-6223, United States of America

³ General Atomics, PO Box 85608, San Diego, CA 92186-5608, United States of America

E-mail: petrov@compxco.com

Received 25 March 2022, revised 27 May 2022

Accepted for publication 22 June 2022

Published 14 July 2022



Abstract

A coupling between two distinctly different codes—one magnetohydrodynamic (MHD) and another kinetic—is achieved and applied for simulation of runaway electron (RE) production. The 3D initial value MHD code NIMROD simulates a DIII-D pure neon shattered pellet injection plasma quench including the propagation and ablation of the fragments, ionization and recombination of the impurities, and the radiated and transported energies. The field data from NIMROD is then used by the bounce-averaged Fokker–Planck Collisional QuasiLinear 3D (CQL3D) kinetic code to simulate the production of REs and their radial transport. The coupling procedure involves mapping of data between different grids and adjustment of the NIMROD toroidal electric field when REs appear. It is shown that without the radial transport, a large RE current is generated, up to 30% of the pre-pellet ohmic current. However, when the radial transport is included in CQL3D, the RE current is reduced to undetectable level, consistent with experiment. Various forms of the radial diffusion are surveyed to determine conditions when the fast electrons would not have time to be accelerated to relativistic energies before they are lost to chamber wall.

Keywords: simulation, runaway electrons, Fokker–Planck, CQL3D, NIMROD

(Some figures may appear in colour only in the online journal)

1. Introduction

Shattered pellet injection (SPI) is considered as the primary candidate for a disruption mitigation system in ITER. In existing tokamaks, other promising methods, such as dispersive shell pellet [1] are also under consideration. Scenarios with pellet injection are notoriously difficult for numerical modeling, as they involve physical processes at different time scales, coexistence of very cold and hot plasmas, large-scale magnetohydrodynamic (MHD) instabilities and strong kinetic effects

in the form of a runaway electron (RE) tail in the distribution function. As a pellet (or its fragments) propagates, the deposition and ionization of impurity material results in a rapid local cooling of plasma on a time scale of order 10–100 μ s, which necessitates a short computational time step on the order of 0.1 μ s or less. At the same time, it may take 1–5 ms for the pellet fragments to reach the plasma center, followed by a current quench phase (CQ) which may take additional 3–10 ms or longer. Thus, a complete modeling should be able to cover about 10 ms or so of plasma discharge, using a small time step during pellet fragments propagation, and it should include all relevant 3D physics in configuration space, such as the evolution of temperature profiles, density profiles of all ionization states of impurity, fast changes in toroidal electric field profile, sudden emergence of magnetic field fluctuations. At the same time, the RE production and their radial transport should

* Author to whom any correspondence should be addressed.



Original content from this work may be used under the terms of the [Creative Commons Attribution 4.0 licence](https://creativecommons.org/licenses/by/4.0/). Any further distribution of this work must maintain attribution to the author(s) and the title of the work, journal citation and DOI.

be described with high fidelity, because the presence of a high energy RE beam is a major menace for ITER (or other large tokamak) operations [2, 3], and mitigation methods need to be understood.

In the present work, we report on a modeling approach involving coupling between two established plasma simulation codes—NIMROD and Collisional QuasiLinear 3D (CQL3D)—which can potentially cover all important aspects of the physics described above. So far, a one-way coupling is achieved, wherein NIMROD simulation is performed first, covering the whole plasma discharge, and then CQL3D uses the time-dependent data from NIMROD to model the emergence of RE current and its radial transport. As a proof-of-principle test, we start with an established NIMROD SPI thermal quench simulations based on the DIII-D discharge shot#160606 [4]. In the experiment, no significant RE current was observed. With the coupled NIMROD-CQL3D simulations, we show that without the radial transport, the RE current can reach 370 kA (30% of the pre-pellet current), but when the radial transport is taken into account the RE current is reduced to nearly zero. Moreover, simple radial diffusion results based on stochastic $\delta B/B$ values from NIMROD overestimates the required radial diffusion to match the experiment, indicating the need for more sophisticated (future work) RE radial transport calculations.

In the coupled modeling, NIMROD simulation covers all physics related to the SPI propagation, including ablation of the impurity material, and its ionization and recombination. Also NIMROD computes time-dependent MHD fluctuations, plasma current (without RE current) and electric field. To couple to CQL3D, this data is averaged over nominal flux surfaces at each time slice and exported to CQL3D. In the CQL3D run, all those profiles are assumed to be unaffected by the emerging RE current, except the electric field, which is adjusted by a special method developed for such types of run, as further described in section 3. The results emphasize that a complete model of RE formation and evolution must include the radial dynamics of the plasma and the fields, as well as effects of the coupled kinetic electron momentum distributions.

A brief description of NIMROD and CQL3D is given in section 2, together with a description of the test case. Section 3 describes the coupling procedure, including the adjustment of electric field when RE current appears. The results of modeling for the case of no radial transport are presented in section 4, followed by section 5 where results of different forms for the radial diffusion coefficient are surveyed. Section 5 contains discussion and summary.

2. Description of the codes and the test case

2.1. NIMROD

NIMROD is a 3D initial value simulation code that leverages advanced implicit and semi-implicit time stepping algorithms, with 2D high order finite elements in the poloidal plane and a finite Fourier series in the toroidal direction, to solve the extended MHD equations [5, 6]. A particle based shattered pellet injector (SPI) model is implemented in the NIMROD code

[7] to study disruption mitigation scenarios. In these NIMROD SPI simulations, we use the pencil beam fragment plume model where the fragments are uniformly distributed along a line that is colinear with their constant velocity trajectories.

To model the impurity driven quench, NIMROD assumes a single fluid model of the plasma but advances a separate continuity equation for each species and impurity charge state. All species have the same temperature and all species are advected by the same velocity. The ionization and radiation modeling in NIMROD is performed using data tables from the KPRAD [8] code. The resistive MHD equations advanced in these simulations are:

$$\frac{\partial n_\alpha}{\partial t} + \nabla \cdot (n_\alpha \mathbf{V}) = S_\alpha + \nabla \cdot D_\alpha \nabla n_\alpha \quad (1)$$

$$\rho_{\text{tot}} \left(\frac{\partial \mathbf{V}}{\partial t} + (\mathbf{V} \cdot \nabla) \mathbf{V} \right) = \mathbf{J} \times \mathbf{B} - \nabla p \quad (2)$$

$$\frac{n_{\text{tot}}}{\Gamma - 1} \left(\frac{\partial T}{\partial t} + \mathbf{V} \cdot \nabla T \right) = -p \nabla \cdot \mathbf{V} - \nabla \cdot \mathbf{q} + Q \quad (3)$$

$$\frac{\partial \mathbf{B}}{\partial t} = -\nabla \times \mathbf{E}, \quad \nabla \times \mathbf{B} = \mu_0 \mathbf{J}, \quad \mathbf{E} = -\mathbf{V} \times \mathbf{B} + \eta \mathbf{J} \quad (4)$$

The runs are initialized with equilibrium fields and currents at specific time step of plasma discharge. No loop voltage is applied in present simulations, assuming perfectly conducting walls. Equation (1) is the continuity equation for α = main ions (i) and for each individual impurity charge state (Z), and D_α is the density diffusion. Each impurity charge state density is advanced along with the main ion density. The electron density is computed by enforcing quasi-neutrality. The NIMROD impurity model has the option of including neutral impurities and neutral main ions. When this option is on, three body recombination is included. Equation (2) is the momentum equation where the mass density is computed from $\rho_{\text{tot}} = m_i n_i + m_e n_e + \sum_Z m_Z n_Z$, and the pressure is $p = n_{\text{tot}} T$, with $n_{\text{tot}} = n_i + n_e + \sum_Z n_Z$. The neutral impurities and neutral ions are included in the sums when the option is on. Equation (3) is the temperature equation, where $\Gamma = 5/3$ is usual ratio of specific heats. The single temperature approximation assumes instant thermalization across all species. Presently, the single temperature is a limit of the NIMROD impurity model. A two temperature model is in development. The temperature advance equation includes anisotropic thermal conduction, as well as ohmic heating and loss due to ionization, recombination and radiation. Bremsstrahlung and synchrotron radiation, although usually small, are also calculated along with the line radiation. The resistivity η in present modeling is based on an analytical fit expression [9] valid for arbitrary collisionality regime, which includes neoclassical trapping effects. The Z_{eff} dependence is included as the impurity material is ionized/recombined to different charge states. This formulation for resistivity is adopted from CQL3D coding, where it is used for synthetic diagnostics and for the feedback procedure for the electric field as described further in section 3.

2.2. CQL3D

CQL3D is a finite-difference bounce-averaged (BA) Fokker–Planck equation solver [10]. It uses flux-conserving differencing between grid cells, and thus conserves particles. In the most general form, the underlying equations can be written as

$$\lambda \frac{\partial}{\partial t} f_0(u_0, \theta_0, \rho, t) = \nabla_{u_0} \cdot \Gamma_{u_0} + \lambda \langle \langle R(f_0) \rangle \rangle + \lambda \langle \langle S \rangle \rangle, \quad (5)$$

$$\nabla_{u_0} \cdot \Gamma_{u_0} = C(f_0) + Q(f_0) + E(f_0) + H(f_0), \quad (6)$$

where f_0 is the time-dependent distribution function found over the momentum-per-mass u_0 and pitch angle θ_0 at the minimum- B point on each flux surface. The generalized radial coordinate ρ labels the flux surface. Toroidal symmetry is assumed. Jacobian $\lambda = |v_{||0}| \tau_b$ is such that $\lambda f_0 d^3 \mathbf{u}_0$ gives the number of particles per unit cross-sectional area of flux tube passing through the outer equatorial plane; $v_{||0} = u_{||0}/\gamma$ is parallel velocity, τ_b is the bounce (or transit) period and $\gamma = \sqrt{1 + u_0^2/c^2}$ is the relativistic factor.

Flux Γ_{u_0} in the 2D momentum space \mathbf{u}_0 includes all processes that can be written in the divergence-of-flux form

$$\begin{aligned} \nabla_{u_0} \cdot \Gamma_{u_0} = & \frac{1}{u_0^2} \frac{\partial}{\partial u_0} \left[\lambda \left(\langle \langle A_{\text{loc}} \rangle \rangle f_0 + \langle \langle B_{\text{loc}} \rangle \rangle \frac{\partial f_0}{\partial u_0} \right. \right. \\ & \left. \left. + \langle \langle \frac{\partial \theta_0}{\partial \theta} C_{\text{loc}} \rangle \rangle \frac{\partial f_0}{\partial \theta_0} \right) \right] + \frac{1}{u_0^2 \sin \theta_0} \frac{\partial}{\partial \theta_0} \\ & \times \left[\lambda \sin \theta_0 \left(\langle \langle \frac{\partial \theta_0}{\partial \theta} \frac{D_{\text{loc}}}{\sin \theta} \rangle \rangle f_0 + \langle \langle \frac{\partial \theta_0}{\partial \theta} C_{\text{loc}} \rangle \rangle \frac{\partial f_0}{\partial u_0} \right. \right. \\ & \left. \left. + \langle \langle \left(\frac{\partial \theta_0}{\partial \theta} \right)^2 \frac{F_{\text{loc}}}{\sin \theta} \rangle \rangle \frac{\partial f_0}{\partial \theta_0} \right) \right], \quad (7) \end{aligned}$$

where $\partial \theta_0 / \partial \theta$ is the transformation coefficient, which in accord with conservation of energy and magnetic moment, and assuming zero-width orbits, has a simple dependence on local pitch angle θ and magnetic field $B(s)$ along orbit,

$$\frac{\partial \theta_0}{\partial \theta} = \frac{B_0 \sin \theta \cos \theta}{B(s) \sin \theta_0 \cos \theta_0}. \quad (8)$$

In the above equations, subscript ‘0’ refers to the minimum- B point ($s = 0$ point, or outboard-midplane point) on each flux surface, while $\langle \langle \dots \rangle \rangle$ represents bounce-averaging along the trapped or passing orbit, plus gyro-averaging. The bounce-averaging approximation is based on assumption of collision time being much greater than the bounce time, and the gyro-period being much smaller than the collision time. It is valid for most of the pre-pellet hot plasma, but may fail when electron temperature drops to a few eV. For such high-collisional plasma, electron toroidal trapping becomes less effective, and the current due to the low velocity bulk part of the distribution is underestimated. This is compensated in CQL3D [11, 12] by a correction based on general-collisionality expression obtained by [9, 13] using the CQLP variation of CQL3D. The missing current is evaluated internally as $\delta J = E \delta \sigma$ where $\delta \sigma = \sigma_{\text{sptz,neo}} - \sigma_{\text{sptz,neo0}}$ and $\sigma_{\text{sptz,neo}}$ is the analytical fit

expression for neoclassical conductivity at arbitrary collisionality, while $\sigma_{\text{sptz,neo0}}$ is its collisionless limit [9, 13]. It should be pointed out that for the RE tail of the distribution, the BA approximation is still valid even when the bulk of distribution is at few eV. We also add the bootstrap current expressions [9, 13] into the total current density.

In equation (7), the local-along-orbit diffusion coefficients B_{loc} , C_{loc} , F_{loc} , and advection-like coefficients A_{loc} and D_{loc} are different for each specific process. For collision operator $C(f_0)$, all these six coefficients can be non-zero, with A_{loc} and D_{loc} corresponding to the frictional drag force. In the RF quasi-linear operator $Q(f_0)$ [14], the A_{loc} and D_{loc} coefficients are absent. For the toroidal electric field operator $E(f_0)$, it is the opposite case—only A_{loc} and D_{loc} coefficients are non-zero, describing the acceleration of particles. Similarly, the synchrotron and bremsstrahlung radiation operator $H(f_0)$ includes just these two coefficients, representing the loss of energy. Expression for each process can be found in the CQL3D manual [10].

The midplane quantities u_0, θ_0, ρ form constants of motion, which for the zero-width orbits ($\rho = \text{const}$ along orbit) are given by $u(s) = u_0$ and $\sin^2 \theta(s) = (B(s)/B_0) \sin^2 \theta_0$. The Liouville theorem gives that $f(u(s), \theta(s), \rho) = f_0(u_0, \theta_0, \rho)$, and thus the distribution is known everywhere on the 2D flux surfaces, given the midplane distribution.

Additionally, the term $\langle \langle R(f_0) \rangle \rangle$ in equation (5) represents a BA radial diffusion/pinch operator. For our particular case under study, the form of the radial diffusion coefficient is discussed in section 5. Also in equation (5), the term $\langle \langle S \rangle \rangle$ corresponds to particle sources or sinks. In present simulations, where CQL3D is advancing the electron distribution function, this term incorporates the large-angle scattering knock-on (avalanche) source [15].

Important for modeling of RE physics, the collision operator $C(f_0)$ in CQL3D uses a relativistic formulation. Also, it includes a fully-nonlinear self-collisional option. However, for present modeling an adjusted nonlinear form is used, in which the zero-order term in an expansion of the distribution function over Legendre polynomials (polynomial P_0 has no dependency on pitch angle) is substituted with the value from the electron Maxwellian distribution with a given temperature and density (based on NIMROD data in present case). Unlike the fully-nonlinear version, this adjusted nonlinear option keeps the bulk of the distribution at the prescribed (time-dependent, in general) background electron temperature, and at the same time it still conserves momentum. Besides the self-collisions, the operator includes collisions with the main ions and with all ionization states of impurity ions, including the neutral state. For interaction of electrons with partially ionized impurity ions and with neutrals, Hesslow’s corrections are added [16]. The impurity ions and neutrals also contribute to the avalanche source (as cold electron target) and to the bremsstrahlung energy loss term.

2.3. Conditions for modeling

For this study, the NIMROD equilibrium is based on DIII-D shot 160606@02990 ms [4] which has a thermal energy of

0.7 MJ and pre-pellet toroidal current of 1.28 MA. The NIMROD simulation uses a poloidal mesh of 72×96 elements with polynomial degree 3 and 22 Fourier modes ($n_\phi = [0, 21]$) in the toroidal direction. The density diffusion is set to $1.0 \text{ m}^2 \text{ s}^{-1}$ and viscosity to $250.0 \text{ m}^2 \text{ s}^{-1}$. A constant anisotropic thermal diffusion model is used with $\chi_\perp = 0.2 \text{ m}^2 \text{ s}^{-1}$ and $\chi_\parallel = 1.0 \times 10^9 \text{ m}^2 \text{ s}^{-1}$.

The nominal SPI injector load consists of a pure neon pellet approximated as a sphere of radius $r_p = 2.0 \text{ mm}$, with a shatter parameter (ratio of pellet radius to fragment radius) of $S_p = 10$. We assume a loss of 80% after shatter, resulting in an injected plume composition of 200 fragments, each fragment with a radius of $r_f = 0.2 \text{ mm}$ and velocity of $v_f = 200.0 \text{ m s}^{-1}$. The injected inventory of impurities is about 2.9×10^{20} neon atoms. The fragments have a linear trajectory along the upper port injector directed at the magnetic axis. The ablated neutral deposition uses a Gaussian shape function with $r_{\text{hw}}^{\text{Gauss}} = 5.0 \text{ cm}$ in the poloidal plane and a von Mises distribution with $\Delta\phi_{\text{hw}}^{\text{vonMises}} = 10\%$ in the toroidal direction [17].

A general progression of this DIII-D shot, as modeled by NIMROD, is illustrated in figure 1(a) which shows the thermal energy along with the total radiated energy and ohmic energy. The thermal quench ends at $t = 1.67 \text{ ms}$ with a radiated efficiency of $\approx 78\%$. NIMROD typically observes a few tenth's of milliseconds between the end of the thermal quench and beginning of the current quench. Also, figure 1(b) shows the trace of plasma current from experimental data (black curve) and from NIMROD simulations (red). The current spike occurs at $t = 1.88 \text{ ms}$ and marks the start of the current quench. In NIMROD simulations, a second spike is observed at $t = 5.48 \text{ ms}$. The first current spike is dominated by an $n_\phi = 1$ event. The second is axisymmetric, dominated by $n_\phi = 0$. More characteristics of this shot are discussed further in section 4.

3. General procedure for coupling

One of difficulties for the coupling of the two codes is that CQL3D relies on externally computed magnetic equilibrium which is expected to contain closed flux surfaces with monotonic increase of magnetic field from the outboard to inboard point on each surface. This requirement is mostly needed for two reasons: (a) to ensure that all orbits associated with a given flux surface pass through the outboard point where the orbits can be characterized by the local pitch angle, and (b) to allow using flux-surface-average (FSA) profiles for density and temperature of background species, which are needed for evaluation of BA collision operator. Radial particle diffusion across the unperturbed flux surfaces then accounts for the effects of electromagnetic turbulence.

NIMROD SPI simulations show flux surfaces deteriorate as soon as the fragments encounter the plasma with a steadily growing envelope of magnetic stochasticity enclosing the collapsing hot core. This progresses until the remnant hot core collapses in a large MHD event accompanied by a radiation spike, completely stochastizing the fields immediately after the end of the thermal quench. As the plasma proceeds into

the current quench and ohmic heating dominates, the flux surfaces begin to heal and reform. However, if the radial perturbation of magnetic field is ignored, the basic structure of approximately closed flux surfaces, and magnetic trapping following those surfaces, remains. To meet the requirement for BA procedure in CQL3D, it was decided to compute the FSA-like profiles in NIMROD by following the computation geometrical mesh ($\Psi_{\text{pol}}, \theta_{\text{pol}}$), which is aligned with unperturbed magnetic equilibrium at pre-pellet time. The normalized radial coordinate is set as $\rho = (R_{\text{out}} - R_{\text{axis}})/(R_{\text{out,LCFS}} - R_{\text{axis}})$, where R_{out} is the major radius at outboard midplane point of a given surface in computational mesh (i.e., a flux surface at pre-pellet time). CQL3D then uses the same unperturbed magnetic surfaces and the same definition of coordinate ρ for BA procedures, at all time steps during simulations. The effects related to magnetic perturbations (which reach peak values of $\delta B/B = 0.05$, according to NIMROD data) are then accounted by a model radial diffusion in CQL3D. This looks like a crude approach for the coupling, but it should be noted that the BA formalism makes the results not sensitive to local variations of plasma parameters and magnetic field fluctuations along a nominal 'surface'. In computing the BA distribution function, the main internal boundary in velocity space is the trapped-passing boundary, which is mostly determined by the $1/R$ variation of the toroidal magnetic field B_ϕ , as the poloidal magnetic field remains much smaller than B_ϕ . The poloidal magnetic field only determines how orbits extend in the $(\phi, \theta_{\text{pol}})$ plane; the toroidal angle is the ignorable coordinate in the CQL3D BA formalism.

For our particular case of SPI in DIII-D shot#160606, NIMROD was providing all relevant profiles in form of data files at 191 time slices covering 6 ms of plasma discharge during the pellet fragments propagation, impurity deposition and ionization, thermal quench and current quench phases. The time slices are not uniform in time, with higher refinement around the TQ event. The data includes temperature and density profiles for electrons and main ions (D^+), and also for all ionization states of impurity (Ne in our case). Also, it includes profiles of FSA current density, parallel electric field and perturbations of the magnetic field $\delta B/B$. These data files are imported and processed by CQL3D at the beginning of each simulation, before advancing the solution for the electron distribution function. The profiles are mapped to the internal CQL3D radial grid, typically much coarser than in NIMROD. The time step in CQL3D is non-uniform and in general can be very large, as CQL3D uses implicit integration. However, to resolve the dynamics of quickly changing profiles in present simulations, the time step was set to $dt = 5 \mu\text{s}$ during the first 320 steps (covering time period $\Delta t = 1.6 \text{ ms}$ of pellet fragments propagation to plasma core), $dt = 2 \mu\text{s}$ for the following 200 steps (covering 0.4 ms around core temperature collapse), and $dt = 20 \mu\text{s}$ for the remaining 170 steps (covering 3.4 ms of current quench phase). The profiles are linearly interpolated in time, from the two nearest time points in the imported data.

It should be underlined that presently NIMROD does not evaluate the production of RE current. Therefore, the values of parallel electric field imported from NIMROD are not accurate when a significant RE current is generated in CQL3D

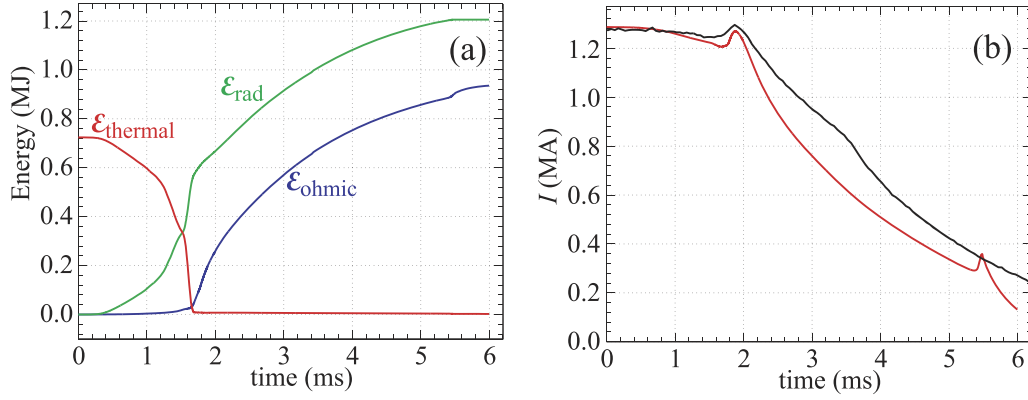


Figure 1. (a) The thermal (decreasing curve), radiated (upper increasing curve), and ohmic (lower increasing curve) energies, simulated by NIMROD for the DIII-D discharge 160606. The radiation efficiency is approximately 78%. The source for the late radiation power is the ohmic heating from the current decay. Plot (b) shows traces of the plasma current from experimental data (upper curve, black) and that from the NIMROD simulation (red).

simulations. In the present one-way coupling scheme, the following feedback procedure is adopted, using the current density $J_{\text{NIMROD}}(\rho, t)$ computed by NIMROD and the RE current density $J_{\text{CQL3D,RE}}(\rho, t)$ computed by CQL3D. For the low RE current case we are considering, it is assumed that the total current density computed by CQL3D should match the one computed by NIMROD, i.e.,

$$J_{\text{CQL3D,ohm}}(\rho, t) + J_{\text{CQL3D,RE}}(\rho, t) + J_{\text{CQL3D,bs}}(\rho, t) = J_{\text{NIMROD}}(\rho, t) \quad (9)$$

where we formally separate the RE from the ohmic part in the distribution function by the critical speed u_c . To obtain the expression for the electric field, we take $J_{\text{CQL3D,ohm}}(\rho, t) = E(\rho, t)\sigma_{\text{sptz,neo}}$, while for the REs the conductivity is much larger than that for ohmic electrons. Then,

$$E(\rho, t) = (J_{\text{NIMROD}}(\rho, t) - J_{\text{CQL3D,RE}}(\rho, t) - J_{\text{CQL3D,bs}}(\rho, t)) / \sigma_{\text{sptz,neo}} \quad (10)$$

In this formula, $\sigma_{\text{sptz,neo}}$ is the Spitzer conductivity with neoclassical correction valid at all collisionality rates [9, 13], evaluated at each ρ and t . As discussed in section 2, the BA formalism used in CQL3D is only valid for low-collisionality limit, so that for a given E field, the distribution function evolves in such a way that the corresponding ohmic part of the current density satisfies $J_{\text{code}} = E\sigma_{\text{sptz,neo0}}$ (in case of no RF and NBI sources), where $\sigma_{\text{sptz,neo0}}$ is the collisionless limit of $\sigma_{\text{sptz,neo}}$. For diagnostic plots (like the plot of total current shown in next section), the ‘missing’ current is added as correction $\delta J = E\delta\sigma = E(\sigma_{\text{sptz,neo}} - \sigma_{\text{sptz,neo0}})$.

In a similar way, there is an option in CQL3D to evaluate and add the bootstrap current $J_{\text{CQL3D,bs}}$, which appears in equations (9) and (10). In present simulations, it was evaluated from analytical fit formulas [9, 13]. As shown further in the next section, the bootstrap current drops to near zero before the REs appear, thus it has a small effect on the value of electric field in the time range where REs are generated. This is confirmed by several test runs where $J_{\text{CQL3D,bs}}$ was not added.

The method described by equation (10) is a feedback procedure because the value of $J_{\text{CQL3D,RE}}$ is produced by electric field at the previous time step. It is clear that when RE current

is zero, the electric field from equation (10) simply follows the one provided by NIMROD. When $J_{\text{CQL3D,RE}}$ emerges, the values of $E(\rho, t)$ from equation (10) are reduced, relative to the values in NIMROD run. From test runs, this method provides a nearly unchanged total current in CQL3D runs, even when I_{RE} replaces 50% of the total current. However, for very high conversion rates, the procedure is not expected to be accurate, and two-way coupling between the codes becomes necessary, with NIMROD using CQL3D-calculated RE current.

4. Results for RE current production with no radial transport

It will be shown in this section that in the case of disabled radial transport in the CQL3D run, the RE current can grow to large values not seen in the actual experiment. The general picture of plasma evolution under the effect of SPI is demonstrated in figure 2. The change of electron temperature at selected radial coordinates reflects the pellet fragments propagation from the plasma edge to the center. The core collapses at $t = 1.60\text{--}1.65$ ms, when the central temperature drops from 2.1 keV to 10 eV. It is seen that in the exterior regions of plasma, $\rho \geq 0.6$, the temperature drops relatively slowly in time, $\tau_T \approx 0.5$ ms. This is important for further discussion on localization of RE current density. The electron density, which is shown in figure 2(b), is increased by factor of two as the pellet fragments propagate, reaching $2.0 \times 10^{14} \text{ cm}^{-3}$ at the plasma center, although during current quench at $t > 2.0$ ms, it is reduced to $1.5 \times 10^{14} \text{ cm}^{-3}$. Besides the density of free electrons, there is a substantial density of bound electrons in neutral or partially ionized impurity, getting to $5 \times 10^{13}\text{--}7 \times 10^{13} \text{ cm}^{-3}$ during CQ.

The change of electric field is shown in figure 3, using two different perspectives. This is the field computed by CQL3D following the RE-adjustment formula in equation (10). The time traces of $E(t)$ in figure 3(a) are plotted for the same selected radial coordinates as $T_e(t)$ in figure 2(a). As the edge temperature drops, the electric field is seen to grow from pre-pellet levels $E(t_0) < 0.1 \text{ V m}^{-1}$ to up to 10 V m^{-1} just before

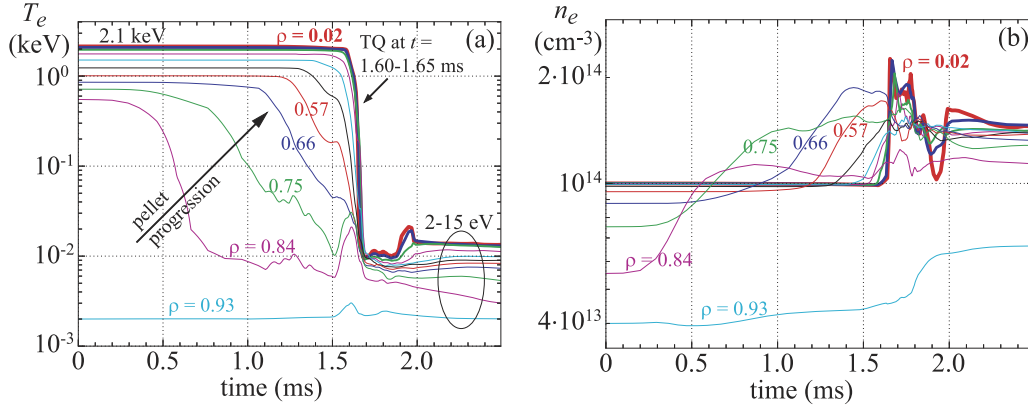


Figure 2. Dynamics of the electron (a) temperature and (b) density in DIII-D shot 160606, as modeled by NIMROD and then mapped to CQL3D radial and time grids. Neon SPI is launched at $t = 0.2$ ms. Traces of $n_e(t)$ and $T_e(t)$ are shown for selected radial points. Only the time range around the TQ [0.0; 2.5 ms] is shown, for clarity.

the core collapse. An interesting feature is seen after the core collapse at $t = 1.65$ ms. At the edge, the field continues to grow up to $30\text{--}50 \text{ V m}^{-1}$, but at the plasma core ($\rho < 0.4$) it drops to 2 V m^{-1} .

An alternative display of the same data is shown in panel (b) of the figure, where the electric field is plotted as a function of radial coordinate ρ and time. The blank areas of the plot correspond to low levels of $E(\rho, t) < 2 \text{ V m}^{-1}$. It is seen that the whole central region at $\rho < 0.4$, $t > 2$ ms, has strikingly low levels of E comparing to neighboring regions at $\rho > 0.4$. The reason is the emergence of highly conductive RE current, which is shown in figure 4, and which is seen to be strongly localized at $\rho < 0.4$. It is exactly in this region of space and time where the electric field is reduced, following the procedure in equation (10).

The absence of RE current at $\rho > 0.4$ could be explained by a relatively slow rate of $T_e(t)$ drop in that region of plasma, as noted in figure 2(a). For the hot-tail mechanism [15] to produce a large population of RE electrons, the cooling of electrons should happen very fast, typically in $\tau_T \approx 1/\nu_0$ time or faster (where ν_0 is the collision frequency for thermal electrons just before the start of the temperature drop). With a slow rate of $T_e(t)$ drop, most of electrons manage to thermalize to the new colder distribution before the critical speed is reduced enough (from the rising $E(t)$ field) to capture those electrons.

The total current computed with CQL3D is shown in figure 5. The RE current (lowest solid line) emerges during TQ, quickly reaching 240 kA at $t = 1.8$ ms, followed by a steady growth to 370 kA by the end of discharge at $t = 5.4$ ms. It is determined by additional test runs that the steady growth is due to the avalanche source. The thin black line corresponds to the current computed by the code $I_{\text{code}}(t)$, including the RE part. As discussed in the previous section, the current calculated from the BA approximation should be corrected with the strongly-collisional thermal part corresponding to $\delta J = E\delta\sigma = E(\sigma_{\text{sptz,neo}} - \sigma_{\text{sptz,neo0}})$. This contribution is plotted with the dashed/blue line, and it shows an opposite trend comparing to the thin/black curve for $I_{\text{code}}(t)$ during $t = [0.2; 1.6]$ ms because a progressively larger number of electrons are entering the collisional regime in the wake of pellet fragments path. Also,

the bootstrap current is shown with the dashed/green line. The adjusted total current (thin/black plus dashed/blue plus dashed/green) is shown with the bold line. It remains nearly stable before the core collapse event, at a level of 1.1–1.2 MA. This part is similar to NIMROD data and experiment, although slightly lower than the peak value of 1.28 MA in NIMROD run. The difference could be explained by the geometric-mesh averaging procedure for profiles that are exported from NIMROD to CQL3D, while in NIMROD, the currents and electric fields are local. Noteworthy, the trace of total current in figure 5 shows two spikes around the core collapse event. One spike is at $t = 1.64\text{--}1.67$ ms, which is exactly when the temperature in the core drops to 10 eV. The second, lower spike is $t = 1.87\text{--}1.91$ ms, and it marks the beginning of current quench. In NIMROD run, only the latter spike is visible at $t = 1.88$ ms, albeit at a higher magnitude of 1.25 MA.

To illustrate physics of the results in this section, figure 6 shows the distribution function at $t = 5.4$ ms, when the RE current is largest. In simulations, the upper boundary in momentum-space mesh was at $u/c \equiv p/m_e c = 79.3$ (40 MeV); the plot shows a smaller portion of this range at $u/c \leq 10$. A characteristic ‘bump-on-tail’ is seen at $u_{\parallel}/c = -3.6$ (1.4 MeV). The positive slope of the distribution function in front of the ‘bump’ favors the excitation of micro-instabilities. The expectation is that whistler wave may grow in magnitude if their parallel phase speed $V_{\parallel} = \omega/k_{\parallel}$ is just below the speed of the ‘bump’ u_{\parallel}/γ (which is at $0.96c$ in this example). The propagating whistler wave may induce pitch-angle scattering of fast electrons in different regions of plasma and inhibit the RE beam to some extent. Substantial growth and effects can occur if the whistler or other wave continues to propagate in the region of wave growth. This is a subject of further study.

5. Crucial effects of radial transport on RE

In NIMROD simulations for this DIII-D shot, large fluctuations of magnetic field are computed as shown in figure 7. Within the time range of 1.4–1.8 ms, the magnitude of magnetic perturbations grows to large levels of $\delta B/B = 0.03\text{--}0.05$, with no closed flux surfaces visible anywhere in the plasma

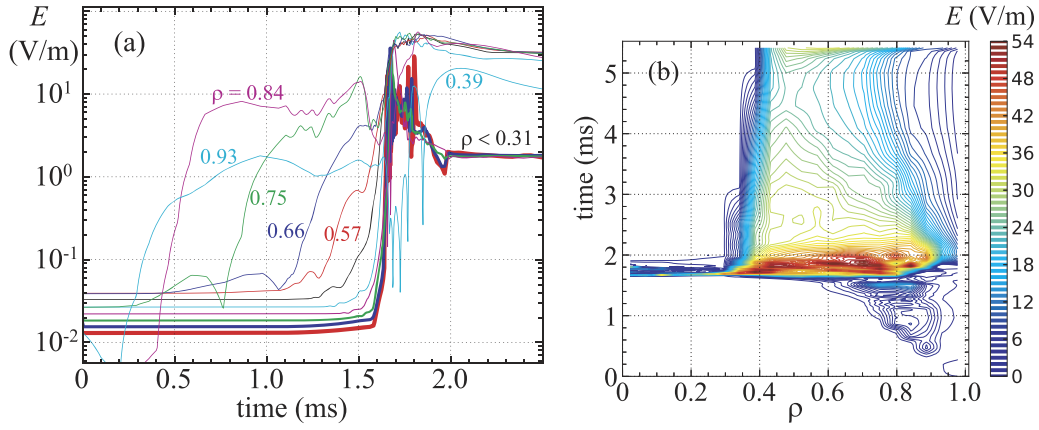


Figure 3. Electric field in the CQL3D run without the RE radial transport—(a) for selected radial points (plotted over short time range, for clarity), and (b) as a function of the normalized radial coordinate and time. From CQL3D, the electric field is small compared to the original data in NIMROD, when RE current appears—mostly at $\rho < 0.4$, $t > 1.8$ ms.

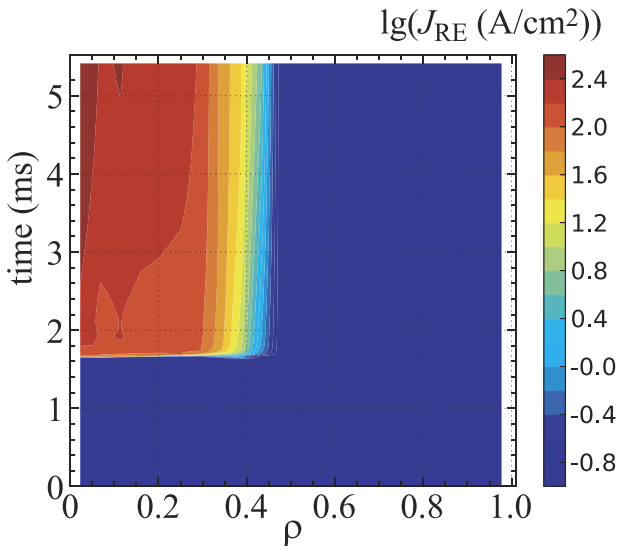


Figure 4. RE current density computed by CQL3D when radial transport is turned off. The RE current mostly appears centrally at $\rho < 0.4$ just after the TQ at $t = 1.65$ ms. It slowly grows during the current quench to 100–400 A cm⁻².

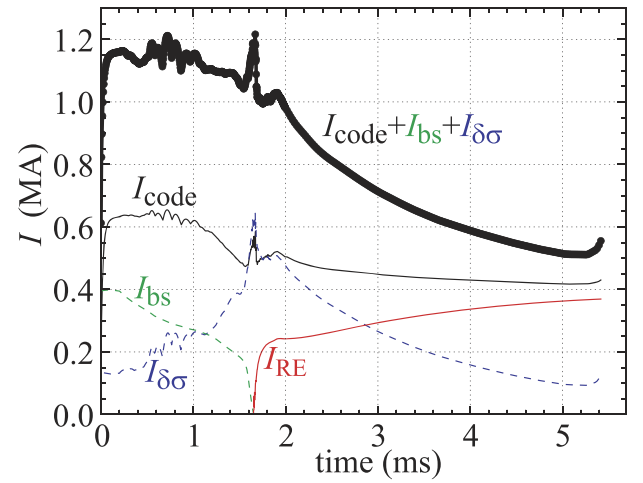


Figure 5. Currents computed with CQL3D; no radial transport in this run. Thin red line corresponds to the RE current, thin/black line—to the current deduced from the whole distribution function (including the RE part), dashed/green—bootstrap current correction, dashed/blue—collisional correction from $E\delta\sigma$, bold/black—the sum of the thin black and the two dashed lines.

cross-section. This implies a strong radial transport for both runaway and thermal electrons.

To account for radial transport of electrons, a model is implemented in CQL3D based on a random-walk approximation [18], adjusted for the pitch-angle dependence [19]. The main justification for using the diffusive-type radial transport in our simulations is that the magnetic flux surfaces become stochastic during TQ, followed by only partial ‘healing’ during CQ phase. We leave discussion on possible reduction of diffusion in presence of magnetic islands to section 6. In addition to the classical expression of [18], a cutoff factor $1/\gamma^n$ is added into the expression for the radial diffusion coefficient, where $\gamma = \sqrt{1 + u^2/c^2}$ is the relativistic factor. As discussed in [15], where $n = 5$ power is deduced from results in [20], the $1/\gamma^5$ factor represents a phase-averaging effect from deviation of electron orbits from magnetic flux surfaces due to

perpendicular drift. It strongly reduces diffusion for electrons with normalized momentum u/c greater than 1.0. A less severe reduction of the radial transport was found by [21] for larger amplitude MHD modes. According to recent numerical study for electrons subject to large-scale magnetic perturbations [22] the finite drift-orbit effects result in a better confinement of electrons traveling in the direction opposite to plasma current (these are typical REs) than electrons traveling in co-current direction, because the former are drifting inwards from a magnetic surface. In the present CQL3D simulation, we perform a survey over the range of power n in $1/\gamma^n$ factor, with value of $n = 0$ corresponding to disregard for such orbital effects.

In general, the expression for radial diffusion coefficient used in present study is

$$D_{\text{tr}} = \frac{L_A}{1 + L_A/\lambda_{\text{mfp}}} |v_{\parallel}| \left(\frac{\delta B}{B} \right)^2 \frac{1}{\gamma^n} \quad (11)$$

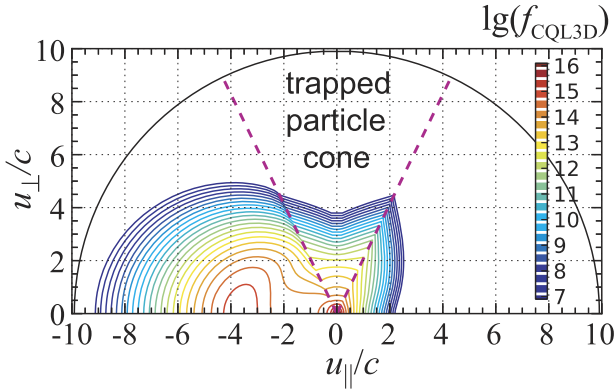


Figure 6. Distribution function computed with CQL3D (in normalized code units) at the selected radial coordinate $\rho = 0.295$ ($R_{\text{out}} = 193.6$ cm), at the last time step corresponding to $t = 5.4$ ms. No radial transport is included in this run. Dashed magenta lines designate trap-passing boundary, which is important for accurate description of total current, including the RE part of the current, since a portion of fast electrons diffuses into the trapped cone and further into the opposite- u_{\parallel} side.

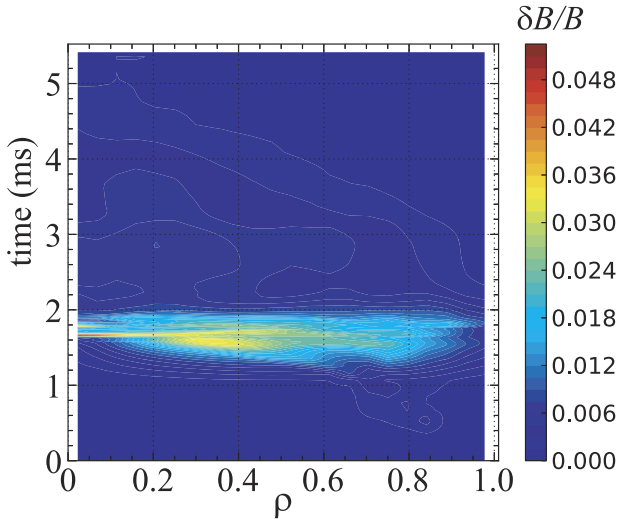


Figure 7. Magnetic field fluctuations computed with NIMROD. The values of $\delta B/B$ reach 0.054 at $t = 1.65$ ms, associated with the temperature collapse at plasma core to 10 eV. At later time range, $t = 2.0$ – 3.0 ms, the fluctuations are smaller, $\delta B/B \approx 0.006$ – 0.008 at $\rho < 0.4$.

where $\lambda_{\text{mfp}} = |v_{\parallel}|/\nu_{ei}$ is the mean free path for electrons, $v_{\parallel} = u_{\parallel}/\gamma$ is the speed along magnetic field line, $\nu_{ei}(\rho, t)$ is the pitch-angle scattering collision frequency, $L_A = \pi q_s R_{\text{axis}}$ is the auto-correlation length, with $q_s(\rho)$ being the safety factor. In most of momentum space, $\lambda_{\text{mfp}} \gg L_A$. It can be noted that for the near-peak values of magnetic fluctuations, $\delta B/B = 0.01$, the radial diffusion coefficient becomes unrealistically high, order of 10^8 cm² s⁻¹ for thermal electrons with $T_e = 2$ keV. In CQL3D simulations, such values of $\delta B/B$ usually result in numerical instability, although it is not always fatal.

A series of numerical runs were performed with CQL3D where the diffusion coefficient in equation (11) as a whole was rescaled by a reducing factor ‘scale_{D_{tr}}’. Effectively, this

means reducing the NIMROD-computed values of $\delta B/B$ by $\sqrt{\text{scale}_{D_{\text{tr}}}}$ at all radial coordinates and all time range. We underline that after rescaling, the shape of radial profiles of $\delta B/B$ magnitude remains unchanged; more importantly, the temporal change of such profiles is kept same as computed by NIMROD. The main purpose of scaling down the level of fluctuations is to obtain the lower limit for fluctuations when the results are still consistent with experiment, i.e., when the RE current is smaller than 1 kA.

The survey of the results for the RE current computed with CQL3D for different reducing factors scale_{D_{tr}} and different values of n in $1/\gamma^n$ factor are presented in figure 8. For each given value of scale_{D_{tr}} and $1/\gamma^n$ representing one numerical run, two values of I_{RE} are plotted—at $t = 2.0$ ms (just after TQ, marked with circles) and $t = 5.4$ ms (marked with stars). There are several important conclusions that can be drawn from this plot. The top pair of blue curves (visually merged into one curve) corresponds to scale_{D_{tr}} = 1×10^{-3} , which means reducing the original values of $\delta B/B$ by a factor of 31.6. This case shows a weak dependence on $1/\gamma^n$ factor. The values of I_{RE} are from 70 kA when using $1/\gamma^0$ factor, to 860 kA when using $1/\gamma^5$ factor. The latter is even larger than 370 kA that was observed in figure 5 in case of no radial transport. This could be interpreted as the improved confinement of RE in presence of radial transport, however, such explanation is hardly meaningful in a diffusive model. The large RE current apparently occurs from the radial transport of a group of electrons from plasma core where they are not in runaway regime yet (compare to [10, figure 5.4]). After being transported to the plasma edge, they fall into runaway regime, because the edge electric field is larger, i.e., the critical speed is lower. Such electrons would be mildly relativistic. For example, electrons with relativistic factor $\gamma = 1.6$ attain the cutoff factor $1/\gamma^5 = 1/10.5$, i.e., they have a 10× better confinement within the model described by equation (11). This value of 10× is consistent with the range of I_{RE} from 70 kA when using $1/\gamma^0$, to 860 kA when using $1/\gamma^5$ factor.

In contrast, the lower curves in figure 8 show a much stronger dependence on $1/\gamma^5$ factor. The bottom pair of curves (green color) corresponds to runs with scale_{D_{tr}} = 0.1. For the $1/\gamma^0$ case (neglecting the drift-orbit effects), the RE current is very small, ranging from 1.8×10^{-5} kA at $t = 2.0$ ms to 4.9×10^{-7} kA at $t = 5.4$ ms (notice— I_{RE} is dropping in time). In the opposite case, when using $1/\gamma^5$ factor, the RE current is larger—from 2.1×10^{-3} kA at $t = 2.0$ ms to 7.8×10^{-3} kA at $t = 5.4$ ms. In this case I_{RE} is growing in time, because of the avalanche source.

Comparing to experimental data for the shot#160606, where only a small $I_{\text{RE}} < 1$ kA is implied, all calculations with scale_{D_{tr}} = 0.1 (with any form of $1/\gamma^n$ factor) are seen to fit the experiment. Using the original NIMROD values, that is, using scale_{D_{tr}} = 1.0, would reduce I_{RE} even further. The previously discussed case of scale_{D_{tr}} = 0.001 (blue curves in figure 8) obviously cannot match the experimental data at any form of $1/\gamma^n$ factor. In this regard, it is interesting to check—at what values of scale_{D_{tr}} (and consequently—what values of $\delta B/B$) it is still possible to get a consistency with experiment. The pair of black curves in figure 8, based on scale_{D_{tr}} = 0.04,

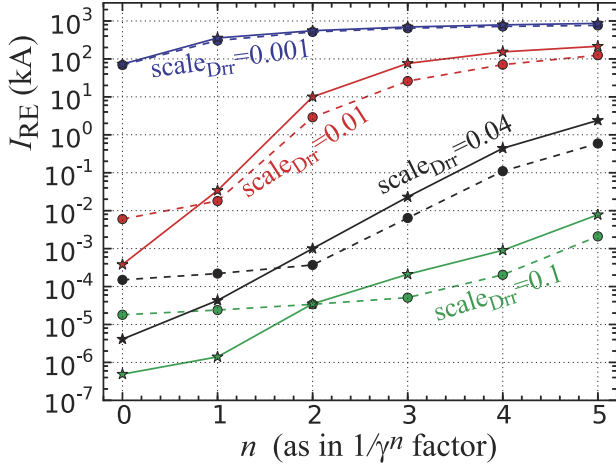


Figure 8. Survey of the RE current computed with CQL3D in the presence of radial diffusion. The horizontal axis is the power n in $1/\gamma^n$ cutoff factor in the radial diffusion coefficient. Color represents the reduction factor $\text{scale}_{D_{\text{rr}}}$ for the whole D_{rr} coefficient. Blue curves correspond to rescaling of D_{rr} by 0.001 (comparing to equation (11)), red curves—to 0.01, black curves—to 0.04, and green curves correspond to rescaling of D_{rr} by a factor 0.1. Each pair of curves with same color corresponds to values of I_{RE} at $t = 2.0$ ms, which is just after TQ (dashed lines with circles) and at $t = 5.4$ ms (solid lines with stars).

seems to be borderline consistent—it yields values of $I_{\text{RE}} = 2.4$ kA when using $1/\gamma^5$ factor, or 0.44 kA when using $1/\gamma^4$ factor.

The pair of red curves, based on $\text{scale}_{D_{\text{rr}}} = 0.01$, can only be consistent with experiment if one uses $1/\gamma^1$ form in equation (11). In this case the RE current is only 3.4×10^{-2} kA at the end of discharge. However, for illustration purpose, we select this case of $\text{scale}_{D_{\text{rr}}} = 0.01$, with a reasonable form $1/\gamma^4$, to discuss other details on RE current density in case of radial transport. The computed current is shown in figure 9. This can be compared with figure 5, where the radial transport is turned off. One noticeable extra feature in figure 9, which was absent in figure 5, is the occurrence of RE current at $t < 1.6$ ms, before the collapse of the plasma core. It appears as a ‘precursor’ RE current, comparing to the major RE current that appears after 1.65 ms. From the figure, it looks like the precursor RE current drops to low values before the main RE current emerges, so it is not important for later dynamics of RE. The precursor RE current exhibits a noise during $t = 1.4$ –1.6 ms, which is from numerical instability discussed earlier. It does not seem to be harmful at later time range, when the values of $\delta B/B(t)$ become smaller.

More insight can be drawn from the plot of $J_{\text{RE}}(\rho, t)$ shown in figure 10, which can be compared to figure 4 where radial transport is disabled. The precursor RE current is generated in the wake of pellet fragments path, where the electric field is increased from the 0.1 V m^{-1} level to 10 V m^{-1} , therefore the critical speed is reduced. As suggested in the earlier discussion, some of nearly-REs in plasma core can be transported to the edge (with high electric field present), where they fall into runaway regime.

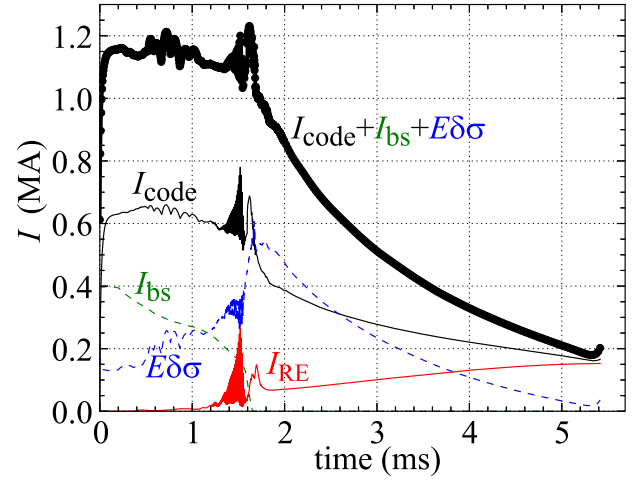


Figure 9. Current computed with CQL3D in a case when the radial transport is present. The thin red line corresponds to the RE current, thin/black line—to the current deduced from first moment of the CQL3D distribution function (including the RE part), dashed/green—bootstrap current correction, dashed/blue—collisional correction, bold/black—the sum of the thin black and the two dashed lines. Here, the radial transport model is based on equation (11) with $1/\gamma^4$ factor.

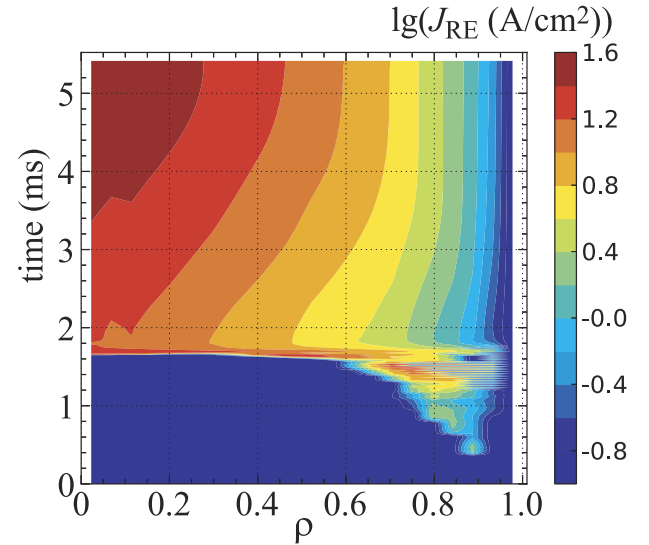


Figure 10. RE current density computed by CQL3D when the radial transport is present, as explained in figure (9). At $t = 5.4$ ms, it reaches 40 A cm^{-2} in the plasma core.

Also noticeable from figure 10 is the wide profile of $J_{\text{RE}}(\rho)$, especially during TQ at $t = 1.65$ ms, when magnetic fluctuations $\delta B/B$ are at their peak values. The RE current density reaches 10 – 20 A cm^{-2} at $t = 1.65$ – 1.70 ms, then drops to lower values, but reemerges after $t = 1.8$ ms. In a separate test run with the avalanche source disabled, the RE current density steadily goes down after $t = 2$ ms.

It is instructive to analyze how different values of D_{rr} can affect the energy of the RE beam. For this purpose we can evaluate the confinement time $\tau_c = a^2/D_{\text{rr}}$ where $a = 62$ cm is the

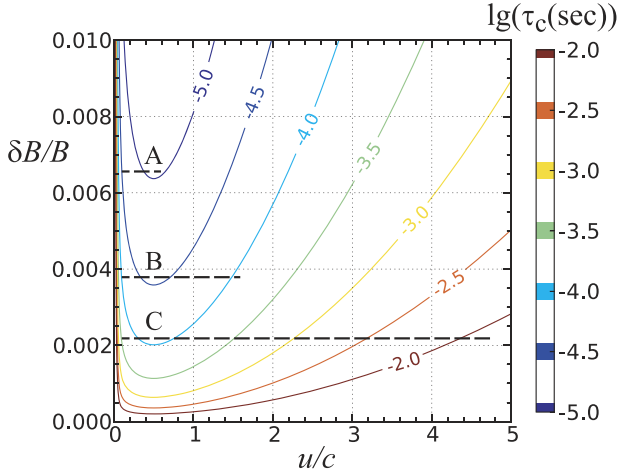


Figure 11. Confinement time τ_c evaluated from equation (11). Dashed lines show the gain in momentum u/c if an electron is accelerated in electric field $E = 80 \text{ V m}^{-1}$ over the time range (A) $1 \times 10^{-5} \text{ s}$, (B) $3.2 \times 10^{-5} \text{ s}$, and (C) $1 \times 10^{-4} \text{ s}$, corresponding to the lowest confinement time along each line.

minor radius of plasma in DIII-D. We also use $L_A = \pi q_s R_{\text{axis}} = \pi \times 2.0 \times 175.7 \text{ cm} = 1104 \text{ cm}$, which is much smaller than the mean-free-path in most of the energy range, and therefore the values of D_{tr} are not sensitive to the particular temperature and density. Also in equation (11), we use $v_{\parallel} \approx v = u/\gamma$, and select the shape of the relativistic cutoff factor as $1/\gamma^4$. The resulting confinement time is plotted in figure 11 as a function of normalized momentum u/c and fluctuation level $\delta B/B$.

The values of τ_c are plotted in logarithmic scale as contour levels ranging from $1.0 \times 10^{-5} \text{ s}$ to $1.0 \times 10^{-2} \text{ s}$. It is seen that for each given magnitude of the fluctuations, the confinement improves at higher energies (higher u/c). For illustration, let us consider how much energy an electron can gain in a given electric field $E = 80 \text{ V m}^{-1}$. For electron with initial momentum $(u/c)_0 = 0.1$ (2.5 keV), the change in momentum during the confinement time $\Delta t = 1.0 \times 10^{-5} \text{ s}$ is only $\Delta(u/c) = 0.47$, thus the ending value is $(u/c)_{\text{end}} = 0.57$, which is 77 keV. This change in u/c is plotted with dashed line ‘A’ in figure 11. Similarly, for confinement time $\Delta t = 3.2 \times 10^{-5} \text{ s}$ ($=10^{-4.5} \text{ s}$), the electron can be accelerated from $(u/c)_0 = 0.1$ to $(u/c)_{\text{end}} = 1.6$ (450 keV). This is plotted with dashed line ‘B’ in the figure. At last, for confinement time $\Delta t = 1.0 \times 10^{-4} \text{ s}$, the electron can be accelerated to $(u/c)_{\text{end}} = 4.8$ (2 MeV), and this is plotted with dashed line ‘C’ in the figure. Actually, in this case, the electron crosses the region with $\tau_c = 1.0 \times 10^{-4} \text{ s}$ only briefly, and then it advances to regions with higher confinement time $1.0 \times 10^{-3} \text{ s}$ – $1.0 \times 10^{-2} \text{ s}$, so that it gets extra time to be accelerated further. Clearly, at fluctuation levels $\delta B/B \approx 0.002$ (0.2%) the electrons have enough time to attain

relativistic energies. In the opposite case of large $\delta B/B \approx 0.007$ (case ‘A’ in the figure), the electrons can get to about 70 keV only. The intermediate case ‘B’ with $\delta B/B \approx 0.004$ approximately corresponds to results shown in figure 9, where the original values of $(\delta B/B)_{\text{NIMROD}}$ are reduced by factor of 10. The RE current is present in this case, although it is quite small—about 70 kA just after TQ. In general, figure 11 shows that there can be no REs detected if fluctuations are higher than $\delta B/B \approx 0.007$, for the particular DIII-D conditions.

6. Discussion and summary

The initial approach to coupling of two distinct codes—one MHD and another kinetic—to form a complete model of RE production and possible dispersal shows promising results. The main challenge is the bounce-average approximation used in CQL3D, which is not always valid in plasmas with low electron temperature and destroyed flux surfaces. These problems are addressed with averaging of NIMROD-computed currents and fields over nominal geometric mesh, and with collisional corrections in CQL3D. A feedback procedure is introduced that modifies the parallel electric field when REs emerge, effectively reducing the field used in CQL3D from the values computed with NIMROD. Such one-way coupling appears valid when the conversion ratio of the initial current to the RE current is below 50%.

It is demonstrated that radial diffusion can play a crucial role in the value of the RE current calculated to exist by the end of plasma discharge. For NIMROD-computed magnetic field fluctuations with peak values reaching $(\delta B/B)_{\text{NIMROD,max}} = 5\%$, it is concluded that the RE current left in the plasma should be near zero. It is likely, however, that the assumption of diffusive-type radial transport is over-simplified. As shown in [23] with orbit-following calculations, the presence of magnetic islands results in advection-dominated radial transport and in effective reduction of the radial diffusion coefficient. Based on our survey with different down-scaled values of $\delta B/B(\rho, t)$, it is found that when using a 1/5 scaling factor for $(\delta B/B)_{\text{NIMROD}}$ data, the RE current still remains at 1 kA or lower (black curves in figure 8), which is estimated to be an upper limit for RE current in the DIII-D shot under this study. Lower values of $\delta B/B$ would result in larger RE current, which was not observed in the experiment, but higher values of $\delta B/B$, including the original values $(\delta B/B)_{\text{NIMROD}}$, would result in a very small or zero RE current, consistent with experiment. This lower limit, $0.2(\delta B/B)_{\text{NIMROD}}$, gives a substantial ‘room’ for accounting the effects of magnetic islands by way of reduction of the Rechester–Rosenbluth diffusion coefficient. Unfortunately, there is no analytical-fit model for such correction. The orbit-following approach for evaluation of advection and diffusion coefficients in a perturbed magnetic field, as described

in [23], is computationally expensive. Our future planned work includes using similar particle-tracing methods in an attempt to describe the effects of islands on radial transport in form of a simplified analytical-fit model.

In our computations, it is also shown that the radial transport can be responsible for the ‘precursor’ of the RE current. This ‘precursor’ becomes detectable at $t \cong 0.4$ ms, $\rho = 0.8$ – 0.9 , and its appearance is attributed to the radial transport of relatively fast electrons from the inner regions of plasma to the edge, where they are ‘caught up’ by high electric field and become REs.

Another observation from the survey with different forms of the radial diffusion coefficient is the high sensitivity of results to the relativistic cut-off factor $1/\gamma^n$ as given in equation (11). This factor becomes important when the REs have time to accelerate to high energies ($\gamma > 2$ – 3 or so). The difference between using $1/\gamma^0$ (i.e., ignoring drift-orbit effects) and $1/\gamma^5$ (including these effects at presumably full capacity) can be a factor of 100 in the resulting RE current (see, for example, red or black curves in figure 8). Although the present CQL3D-NIMROD model cannot calculate the radial transport self-consistently and must rely on a prescribed form for D_{tr} , these results urge an in-depth study of a more versatile expression for radial electron transport coefficients in magnetic turbulence, specifically for fast electrons at relativistic energies. Such study can be done with test-particle codes as that e.g. in [22, 23].

Acknowledgments

The authors acknowledge helpful discussions with Drs. Y.Q. Liu and V.A. Izzo. This material is based upon work supported by the U.S. Department of Energy, Office of Science, Office of Fusion Energy Sciences, using the DIII-D National Fusion Facility, a DOE Office of Science user facility, under Award(s) DE-SC0018109, DE-SC0016452, DE-FG02-95ER54309, DE-FG02-04ER54744 and DE-FC02-04ER54698. This research used resources of the National Energy Research Scientific Computing Center (NERSC), a U.S. Department of Energy Office of Science User Facility located at Lawrence Berkeley National Laboratory, operated under Contract No. DE-AC02-05CH11231. This report was prepared as an account of work sponsored by an agency of the United States Government. Neither the United States Government nor any agency thereof, nor any of their employees, makes any warranty, express or implied, or assumes any legal liability or responsibility for the accuracy, completeness, or usefulness of any information, apparatus, product, or process disclosed, or represents that its use would not infringe privately owned rights. Reference herein to any specific commercial product, process, or service by trade name, trademark, manufacturer, or otherwise does not necessarily constitute or imply its endorsement, recommendation, or favoring by the United States Government or any agency thereof. The views and

opinions of authors expressed herein do not necessarily state or reflect those of the United States Government or any agency thereof.

ORCID iDs

Yu.V. Petrov  <https://orcid.org/0000-0003-4612-1951>

L.L. Lao  <https://orcid.org/0000-0003-1937-2675>

References

- [1] Izzo V.A. 2020 *Nucl. Fusion* **60** 066023
- [2] Lehnen M. *et al* 2015 *J. Nucl. Mater.* **463** 39–48
- [3] Breizman B.N., Aleynikov P., Hollmann E.M. and Lehnen M. 2019 *Nucl. Fusion* **59** 083001
- [4] Shiraki D., Commaux N., Baylor L.R., Eidietis N.W., Hollmann E.M., Lasnier C.J. and Moyer R.A. 2016 *Phys. Plasmas* **23** 062516
- [5] Sovinec C.R. *et al* 2004 *J. Comput. Phys.* **195** 355
- [6] Sovinec C.R. and King J.R. 2010 *J. Comput. Phys.* **229** 5803
- [7] Kim C.C., Liu Y., Parks P.B., Lao L.L., Lehnen M. and Loarte A. 2019 *Phys. Plasmas* **26** 042510
- [8] Whyte D.G. *et al* 1997 *Proc. 24th European Conf. Controlled Fusion and Plasma Physics (European Physical Society, Petit-Lancy, 1997)* (Berchtesgaden, Germany) 9–13 June 1997 vol 21A (http://libero.ipp.mpg.de/libero/PDF/EPS_24_Vol3_1997.pdf)
- [9] Sauter O., Angioni C. and Lin-Liu Y.R. 1999 *Phys. Plasmas* **6** 2834
- [10] Harvey R.W. and McCoy M.G. 1992 1992 The CQL3D Fokker–Planck code *Proc. IAEA Technical Committee Meeting on Advances in Simulation and Modeling of Thermonuclear Plasmas (International Atomic Energy Agency, Vienna, 1993)* (Montreal, Canada) 15–17 Jun 1992) p 489 (available through USDOC/NTIS No 93002962). Also available with corrections at (www.compxco.com/cql3d_manual.pdf)
- [11] Harvey R.W., Petrov Y.V., Kim C.C., Forest C.B., Lao L.L. and Parks P.B. 2019 *Nucl. Fusion* **59** 106046
- [12] Harvey R.W., Petrov Y.V., Bonoli P.T., Shiraiwa S. and Parks P.B. 2021 CQL3D-GENRAY simulations of suppression of impurity-induced current quench using LH current drive in C-Mod (Spain Sitges June 21–25, 2021) vol 45A *47th European Physical Society* (<http://ocs.ciemat.es/eps2021pap/pdf/P3.1053.pdf>)
- [13] Angioni C. and Sauter O. 2000 *Phys. Plasmas* **7** 3122
- [14] Stix T.H. 1992 *Waves in Plasmas* (New York: AIP)
- [15] Harvey R.W., Chan V.S., Chiu S.C., Evans T.E., Rosenbluth M.N. and Whyte D.G. 2000 *Phys. Plasmas* **7** 4590
- [16] Hesslow L., Embréus O., Wilkie G.J., Papp G. and Fülöp T. 2018 *Plasma Phys. Control. Fusion* **60** 074010
- [17] (https://en.wikipedia.org/wiki/Von_Mises_distribution)
- [18] Rechester A.B. and Rosenbluth M.N. 1978 *Phys. Rev. Lett.* **40** 38
- [19] Harvey R.W., McCoy M.G., Hsu J.Y. and Mirin A.A. 1981 *Phys. Rev. Lett.* **47** 102
- [20] Mynick H.E. and Strachan J.D. 1981 *Phys. Fluids* **24** 695
- [21] Tokuda S. and Yoshino R. 1999 *Nucl. Fusion* **39** 1123
- [22] Liu Y.Q., Parks P.B., Paz-Soldan C., Kim C. and Lao L.L. 2019 *Nucl. Fusion* **59** 126021
- [23] Särkimäki K., Hirvijoki E., Decker J., Varje J. and Kurki-Suonio T. 2016 *Plasma Phys. Control. Fusion* **58** 125017